catalysts

MDPI

Article

Effect of N-Doped Carbon on the Morphology and Oxygen Reduction Reaction (ORR) Activity of a Xerogel-Derived Mn(II)O Electrocatalyst

Shaik Gouse Peera [1,*,†], Ravindranadh Koutavarapu [2,†], P. Siva Prasada Reddy [3], Ganesh Koyyada [4,5], Abdullah N. Alodhayb [6], Saravanan Pandiaraj [7], Seung Won Kim [1] and Mohan Rao Tamtam [8,*]

1 Natural Science Research Institute, College of Natural Sciences, Keimyung University, 1095, Dalseo-gu, Daegu 42601, Republic of Korea; swkim@kmu.ac.kr
2 Physics Division, Department of Basic Sciences and Humanities, GMR Institute of Technology, Razam 532127, Andhra Pradesh, India; ravindranadh.k@gmrit.edu.in
3 MLR Institute of Technology, Dundigal, Hyderabad 500043, Telangana, India; sivaprasad@mlrit.ac.in
4 Department of Chemical Engineering, Yeungnam University, 214-1 Daehak-ro 280, Gyeongsan 38541, Gyeongbuk-do, Republic of Korea; ganeshkoyyada@gmail.com
5 Department of Chemistry, School of Sciences, SR University, Warangal 506371, Telangana, India
6 Department of Physics and Astronomy, College of Science, King Saud University, Riyadh 11451, Saudi Arabia; aalodhayb@ksu.edu.sa
7 Department of Self-Development Skills, King Saud University, Riyadh 11451, Saudi Arabia; psaravanan.c@ksu.edu.sa
8 Data Science Lab, Department of Information and Communication Engineering, College of Mechanical and IT Engineering, Yeungnam University, Gyeongsan 38541, Republic of Korea
* Correspondence: gouse@kmu.ac.kr (S.G.P.); mohantamtam@yu.ac.kr (M.R.T.)
† These authors contributed equally to this work.

Citation: Peera, S.G.; Koutavarapu, R.; Prasada Reddy, P.S.; Koyyada, G.; Alodhayb, A.N.; Pandiaraj, S.; Kim, S.W.; Tamtam, M.R. Effect of N-Doped Carbon on the Morphology and Oxygen Reduction Reaction (ORR) Activity of a Xerogel-Derived Mn(II)O Electrocatalyst. *Catalysts* **2024**, *14*, 792. https://doi.org/10.3390/catal14110792

Academic Editors: Loreta Tamasauskaite-Tamasiunaite and Virginija Kepeniene

Received: 9 October 2024
Revised: 4 November 2024
Accepted: 4 November 2024
Published: 6 November 2024

Abstract: This work synthesizes a xerogel from a sol–gel synthesis strategy and supports it on N-doped carbon support from spent coffee biomass (Mn(II)O/N-CC, hereafter MnO) as an efficient oxygen reduction reaction (ORR) catalyst in alkaline electrolytes. The effects of N-CC carbon content on MnO nanoparticle size, dispersion, distribution, morphology, and electrochemistry on ORR are discussed. The SEM and TEM measurements show that increasing the N-CC content during the MnO gelation reaction improved MnO dispersion and particle size during thermal treatment, increasing the ORR's electrochemical active surface area. Several physiochemical and electrochemical characterizations show a clear relationship between N-CC catalysts and ORR activities. The best catalyst, MnO/N-CC-5, had an even distribution of 27 nm MnO nanoparticles on the N-CC support. The MnO/N-CC-5 catalyst had almost identical ORR kinetics and stability to those of the state-of-the-art Pt/C catalyst in 0.1 M KOH electrolytes, losing only 10 mV in half-wave potential after 5000 potential cycles and retaining 96% of current for over 10 h of continuous chronoamperometric stability. By measuring the electrochemical active surface areas of various catalysts by cyclic voltammetry at different scan rates and measuring the double layer capacitance (C_{dl}) and ECSA, MnO/N-CC-5 catalysts were shown to have enhanced ORR activity. The XPS analysis explains the ORR activity in terms of the Mn^{3+}/Mn^{4+} ratio, and a mechanism was proposed. These findings suggest that the MnO/N-CC-5 catalyst could be a cathode catalyst in fuel cells, biofuel cells, metal–air batteries, and other energy conversion devices.

Keywords: xerogel; MnO nanoparticles; oxygen reduction reaction; N-doped carbon; biomass; effect of particle size; effect of carbon support

1. Introduction

There is a growing demand for high energy as a result of the ever-increasing population and industrialization that is occurring all over the world. It is highly desirable to look for

sustainable energy sources that have a smaller impact on the carbon footprint [1–3]. Energy production and conversion through electrochemical reactions have recently gained tremendous interest in forms such as batteries, solar cells, hydrogen production, hydrogen generation and conversion, etc. [4–8]. Among energy conversion technologies, hydrogen energy conversion by fuel cells is interesting, particularly for transportation applications [9,10]. For continuous energy production through fuel cells, the kinetics of electrochemical reactions such as the hydrogen oxidation reaction (HER) and oxygen reduction reaction (ORR) by electrocatalysts on anodes and cathodes, respectively, are the important deciding factors. Between these two reactions, the sluggish, cathodic ORR is a major limiting factor and therefore requires electrocatalysts with high ORR activity [11,12]. To date, electrocatalysts have been made using noble metals, especially Pt-nanoparticles supported on high-surface-area carbon (Pt/C) and their alloyed catalysts with transition metals (Pt-Co, Pt-Fe), which are considered as the best choice in mediating faster ORR kinetics and therefore serve as a standard catalyst for cathodic ORR reactions [13,14]. Despite their superb ORR activity, the successful commercialization of fuel cells is limited by their high cost, scarcity, and poor stability in acidic and alkaline conditions [15,16]. Therefore, for the past two decades, research has been focused on the search for alternative electrocatalysts from Pt/C that are made of cheap, earth-abundant metals, which has gained tremendous interest among the materials and electrochemists [17]. In particular, electrocatalysts made of 3*d*-transition metals such as Fe, Co, Ni, Cu, and Mn in combination with N-doped carbon are considered as the most promising electrocatalysts that can serve as alternatives to the traditional Pt/C catalysts [18,19]. This is due to their efficiency in interacting with adsorbed oxygen via unoccupied 3*d* orbitals, assisted by the high electronic conductivity of the N-doped carbon, which promotes electronic conduction and enhances ORR kinetics [20]. Among the 3*d*-transition-metal-based catalysts, Fe and Co in combination with N-doped carbons have been extensively investigated because of their excellent ORR activity in comparison with Pt/C in both acidic and alkaline electrolytes [21]. In synthesized catalysts, Fe and Co metals are either in an atomically dispersed state on the N-doped carbons or clusters/nanoparticles of carbides/nitrides/oxides, both of which have been proposed as ORR active sites [22,23]. Though excellent catalysts of Fe and Co have been synthesized, these catalysts suffer from the limitations of poor stability due to leaching of the active metals from the catalysts and Fenton-type reactions mediated by Fe-based catalysts, which produce unwanted H_2O_2 as a byproduct, which further produces $^{\bullet}OH$ [24]. Between these, Fenton-type reactions possess a particular issue, as the produced H_2O_2 and $^{\bullet}OH$ degrade the catalyst layer, promote carbon support corrosion, delaminate the Fe from the active sites, and promote the rapid degradation of the Nafion membrane. Consequently, the investigation of non-Fenton-reactive metals such as copper, ruthenium, and manganese is regarded as the most suitable option for reducing the catalyst degradation that occurs as a result of Fenton-associated reactions and, consequently, for enhancing the overall activity and stability of the catalyst [25–27].

Among the non-Fenton-reactive metals, Mn- and Mn-oxide-based catalysts are particularly interesting because of the ability of Mn to interchange among $Mn^{2+} \leftrightarrow Mn^{3+} \leftrightarrow Mn^{4+}$ oxidation states, enabling molecular chemisorption of O_2, which would facilitate O=O bond breaking and improve the O_2 reduction kinetics by reducing the activation energy required for ORR [28]. However, owing to their abundance, cheap cost, and rich redox chemistry, materials based on manganese have attracted a lot of attention [29]. In particular, the H_2O_2-associated drawbacks are mitigated by Mn-based catalysts, as the Mn^{3+}/Mn^{4+} redox couple is recognized for its effective $^{\bullet}OH$ scavenging capacity, thus enhancing the stability of Mn-based catalysts [30,31]. Despite fast electrocatalytic ORR activity, Mn-oxide-based catalysts suffer from poor electronic conductivity [32]. Because there are many possible Mn valences (ranging from 0 to +7), Mn aggregates form easily during high-temperature carbonization, even when the Mn content is low. This makes it very important to control the particle size and sintering during high-temperature treatment to retain a high electrochemically active surface area available to the ORR reaction [33]. To address these drawbacks,

in general, Mn-oxide nanoparticles are supported on carbon materials, which provide sufficient surface area to host nanoparticles and provide them an electronic conduction pathway [34]. Further, doping the carbon support with heteroatoms such as N further improves the electronic conductivity of the catalyst, and N-doped carbon provides strong metal–support interaction between Mn-oxide nanoparticles and N-doped carbon, therefore enhancing the overall stability of the catalyst [35,36]. In this regard, several types of carbon nanomaterials have been introduced aiming to improve catalyst ORR activity and stability such as CNTs, graphene, carbon black, graphitic-carbon nanofibers, etc. [37–39]. Recently, synthesizing porous carbons from renewable biomass has received special attention for several reasons, such as their easy availability and cheap cost. In particular, the accumulation of biomass has become a serious threat to the environment's sustainability [40–42]. In addition, biomass can be obtained from a wide variety of renewable sources as waste products. The use of biomass reduces the dependence on the traditional methods used for synthesizing carbon nanomaterials and can reduce landfill waste because of the ecofriendly nature of the synthesis process, which requires just washing and pyrolysis steps to prepare porous, high-surface-area carbon for various applications [43]. In this regard, the biomass derived from spent coffee grounds has attracted immense attention. Approximately 90% of spent coffee waste is produced for every 1 kg of fresh coffee used, leading to the production of tons of spent coffee biomass, which eventually goes to landfills [44]. From the landfills, it undergoes environmental bacterial degradation, leading to the release of various greenhouse gases, such as methane and CO_2. Therefore, converting the waste biomass into value-added products such as porous carbon reduces not only greenhouse gas emissions but dependence on petroleum products to produce carbon nanomaterials [45].

Inspired by the aforementioned and in our prior research [46], we have synthesized porous N-doped carbon from spent coffee grounds, in which melamine is used as the N source to produce N functionalities in the derived N-doped carbon. Then, the porous N-doped carbon is used as support to immobilize MnO nanoparticles. The MnO nanoparticles are synthesized from the thermal treatment (900 °C) of Mn-Xerogel, which is made from the gelation reaction between glucose and potassium permanganate aqueous solution in the presence of porous N-doped carbon (MnO/N-CC-900). The as-obtained MnO/N-CC-900 catalyst is assessed for its ORR in 0.1 M $HClO_4$ solution and the half-wave potential of 0.69 V is achieved. In contrast to our previous work, in this work, we have investigated the effect of N-doped carbon content on the morphology and the electrocatalytic ORR activity of xerogel-derived MnO nanoparticles. The aim of this work is to investigate the effect of varying N-doped carbon concentration in the catalyst layer on MnO nanoparticle size, dispersion and distribution, stabilization of MnO nanoparticles, resulting in increased electrochemical active surface area (ECASA), enhanced electronic conductivity of the catalyst, resulting in faster electron transfer during the ORR. With this consideration, we have synthesized the Mn-Xerogel with varying contents of N-doped carbon added in situ during gelation reaction. The resulting Mn-Xerogel/N-doped carbon mixture is then subjected to thermal treatment at 900 °C, resulting in the formation of MnO/N-doped carbon catalyst. The obtained catalysts are then subjected to physicochemical characterization such as XRD, SEM and TEM studies. Further, the MnO/N-doped carbon catalyst is electrochemically characterized for the oxygen reduction reaction in alkaline (0.1 M KOH) electrolytes. Cyclic and linear sweep voltammetry studies were used to investigate the effect of MnO nanoparticle size and distribution, while a potential cycling test was used to investigate the catalyst's stability. It was observed that the nitrogen-doped carbon content significantly influences the size and dispersion of MnO nanoparticles; as the nitrogen-doped carbon support increases, the size of the MnO nanoparticles gradually decreases, thereby proportionately enhancing the electrochemically active surface area and, consequently, the ORR activity.

2. Results and Discussion

2.1. Crystallographic and Morphological Analysis of N-Doped Carbon-Supported MnO Nanoparticles

The washed spent coffee waste is mixed with the N-rich organic ligand, i.e., melamine. During the sonication and magnetic stirring, the melamine adsorbs on the surface of the carbon. When the mixture is subjected to pyrolysis, the adsorbed melamine decomposes into g-C_3N_4 at the temperature of around 350 °C and then with further increase in the temperature, the g-C_3N_4 eventually decomposes into NH_3 species, which acts as source of N, which then integrates into the carbon matrix. Nitrogen doping occurs in the carbon framework through active sites created when unstable oxygen functionalities decompose during graphitization of the carbon. The amount of melamine added to the carbon matrix can be varied to achieve the best N content that can be incorporated. In our previous studies, we have optimized the amount of N in the carbon matrix, with the mass ratio of 1:1, i.e., carbon–melamine [46]. Therefore, in this study, we have directly chosen the optimized mass ratio-derived N-CC and used it as support to deposit the MnO nanoparticles (Figure 1a,b). A sol–gel synthesis strategy leads to the formation of gel when N-CC and D-Glucose solutions are added to an aqueous solution of $KMnO_4$. In this reaction, $KMnO_4$ acts as oxidizing agent, whereas D-glucose acts as a reducing agent, by giving electrons to the MnO_4^- ions. When mixed and agitated with a glass rod, an exothermic reaction takes place (which can be felt by touching the outer surface of the beaker and feeling the beaker is hot). $KMnO_4$ oxidizes the D-Glucose during this MnO_4^- reduction to form MnO_2, and eventually, the D-glucose oxidizes to other forms of oxidized species. When mixed, approximately within 2 to 3 min, the solution instantaneously turns to a gel of MnO_2. The obtained interconnected MnO_2 gel from the colloidal system typically entraps a substantial quantity of H_2O within its structure, which is periodically removed from the gel. The gel within the beaker is transferred into the hot-air oven and the temperature is increased to ~60 °C, facilitating the gradual, natural evaporation of the water, and resulting in the gel drying and contracting to form a xerogel. This entire process occurs in the presence of N-doped carbon, which is already added to the glucose solution; therefore, the N-CC traps in the interconnected gel in situ, during the formation of the xerogel. And when the N-CC-Mn-xerogel is subjected to the thermal treatment at 900 °C, the Mn-oxide nanoparticles are deposited on to the N-CC carbon support (Figure 1c). Furthermore, the N-doped carbon content helps in stabilizing the MnO nanoparticles during heat treatment at high temperatures. With the increase in the content of N-doped carbon content, more and more carbon is trapped inside the gel, which helps in mitigating the coalescence and agglomeration of MnO nanoparticles during the thermal treatment at high temperatures (Figure 1d). This helps in reducing the particle size and improving the dispersion of MnO nanoparticles, increasing electrochemically active surface area and thus enhancing ORR activity, as we noticed in the experimental findings discussed below.

Figure S1a shows the XRD patterns of washed, spent coffee waste and pyrolyzed coffee waste compounds. It is seen that the obtained spent coffee waste shows poor graphitization along with some impurities. In contrast, the pyrolyzed spent coffee waste shows more graphitic character, as indicated by the shift in the graphitic peak corresponding to C (0 0 2) from 2θ of 20° → 25°. This indicates that pyrolysis helps structurally transform amorphous carbon into graphitic carbon. High-temperature pyrolysis helps to decompose amorphous and unstable carbon phases and helps rearrange the carbon atoms into more ordered, graphitic carbons. This graphitization also enhances the aromatic nature of the carbon matrix and thus helps in enhancing the electronic conducting nature of the carbon. In addition, during pyrolysis, decomposition of the melamine occurs at around ~350 °C, leading to the formation of g-C_3N_4. Upon further increase in the temperatures, the decomposition of the g-C_3N_4 leads to the formation of N-containing species, which includes ammonia and other radicals of N, which reacts with the carbon matrix at defect sites or edge carbons, leading to the doping of N in the carbon matrix in various forms, including pyridinic-N, pyrrolic-N and graphitic-N species and oxidized-N species, as identified from

the XPS analysis. Figure 2 shows the XRD patterns of the MnO nanoparticles deposited on N-CC carbon. All the catalysts showed the patterns associated with the MnO at 35.0, 40.5, 58.7, 70.0, and 73.9°, corresponding to the (1 1 1), (2 0 0), (2 2 0), (3 1 1), and (2 2 2) planes, respectively. (PDF#07-0230, PDF#04-0326) indicates MnO cubic and orthorhombic phase structures, respectively [47]. The existence of two phases of MnO may be ascribed to the capacity of MnOx to generate diverse crystal structures with various phases, influenced by both thermodynamic and kinetic factors that dictate the formation of cubic versus orthorhombic phases. The stable form of MnO is typically cubic at lower temperatures; however, during thermal treatment, the cubic phase may transform into an orthorhombic phase. The cubic phase is typically thermodynamically stable, while the orthorhombic phase is kinetically stable. Although cubic MnO is thermodynamically favored, the thermal treatment conditions (temperature, heating rate, and N_2 atmosphere) may not allow for equilibrium. Fast heating or non-equilibrium gel-to-solid conversion stabilizes both phases. This allows cubic and orthorhombic phases to coexist instead of a stable cubic phase. Further, in our previous study, we have previously established a temperature-dependent phase transformation of Mn_xOy that can yield different phases based on the heat treatment temperatures [46]. From our previous study, we have chosen the temperature of 900 °C, at which the MnO_2 transforms into MnO via Mn_2O_3 and Mn_3O_4 (temperatures below 700 °C) phases, i.e., $MnO_2 \rightarrow Mn_2O_3 \rightarrow Mn_3O_4 \rightarrow MnO$ [48]. Though all the MnO/N-CC catalysts exhibited similar diffraction patterns, one can notice a significant change in the intensity of the peaks, following a pattern based on the amount of N-doped carbon added during the gel formation. It is observed that the intensity of the diffraction peaks steadily decreases with an increase in the N-carbon content. This clearly indicates that the crystal size of the MnO nanoparticles consistently decreases with an increase in the N-carbon content. The crystal sizes of the MnO nanoparticles are calculated based on the Scherrer equation by considering the high-intensity peak at 40.5°, corresponding to the (2 0 0) phase of the MnO nanoparticles. The calculated crystal sizes of MnO nanoparticles are ~47, 41, 36, 32, 27, 20 nm for the catalyst corresponding to the N-carbon content of 50, 100, 200, 300, 400, 500 mg, respectively. One can notice that the crystal size of the MnO nanoparticles consistently decreases with the increase in N-carbon content. These observations are further corroborated by the examination of the morphology of the MnO/N-CC catalysts by SEM and TEM measurements.

Figure 3 shows the SEM images of the MnO/N-CC catalysts. The SEM images show a dense distribution of MnO nanoparticles on the N-CC support. It is seen that in catalysts with a smaller quantity of N-CC carbon support, MnO nanoparticles are seen to be agglomerated into large particles. However, as the N-CC content increases, the MnO nanoparticle aggregation is found to be decreased and MnO nanoparticles are spatially apart from each other, leading to an even distribution of MnO nanoparticles with smaller size. Similar observations are also made from TEM measurements, as shown in Figure 4. Highly agglomerated MnO nanoparticles have been observed for MnO/N-CC-1 and 2 catalysts. For MnO/N-CC-3 and 4 catalysts, the agglomeration is lessened and MnO nanoparticles are spatially apart from each other. Interestingly, for the MnO/N-CC-5 and 6 catalysts, it is seen that MnO nanoparticle size has been reduced to a significant extent and the MnO nanoparticles are evenly distributed with nearly no visible agglomerations. This indicates that the N-doped carbon support plays a significant role in mitigating MnO nanoparticle agglomeration and helps to reduce the MnO nanoparticle size, thereby enhancing the electrochemically active surface area of the catalyst, and hence the ORR activity. This observed phenomenon can be explained as follows. With increasing carbon content, more and more of the carbon surface is available for holding MnO nanoparticles; therefore, the MnO nanoparticles evenly distribute on the carbon surface, mitigating the agglomeration during high-temperature treatment, by enhancing the physical space between MnO nanoparticles [49]. In addition, the -N doping sites act as anchoring sites for metal nanoparticles, therefore promoting nucleation and stabilization during the thermal treatment [50]. The higher N-CC means increased available nucleation sites on the large carbon surface, successfully inhibiting the

coalescence and Ostwald ripening of nanoparticles during high-temperature treatment and leading to smaller MnO nanoparticles with high N-doped carbon content [51]. The high electronic density around -N doped functionalities exerts strong metal–support interaction, which could additionally reduce the surface diffusion of Mn species, limiting the chances of MnO nanoparticle coalescence during high-temperature treatment [52]. Overall, the reduction in MnO particle size results in higher electrochemically active surface area available for reacting with gaseous O_2 during ORR, thereby improving ORR activity. Higher content of N-CC also means increased density of -N dopants, which additionally provides high electronic conductivity to the MnO active sites during ORR, thus facilitating the enhancement of ORR kinetics [53]. The overall synergistic effect of -N doped carbon and MnO nanoparticles leads to enhanced dispersion, prevention of coalescence and Ostwald ripening during the high-temperature treatment of xerogel-N-CC, and improved electronic transfer and stabilization of MnO nanoparticles on N-doped sites enhances the ORR activity and stability under electrochemical conditions, as experimentally observed below.

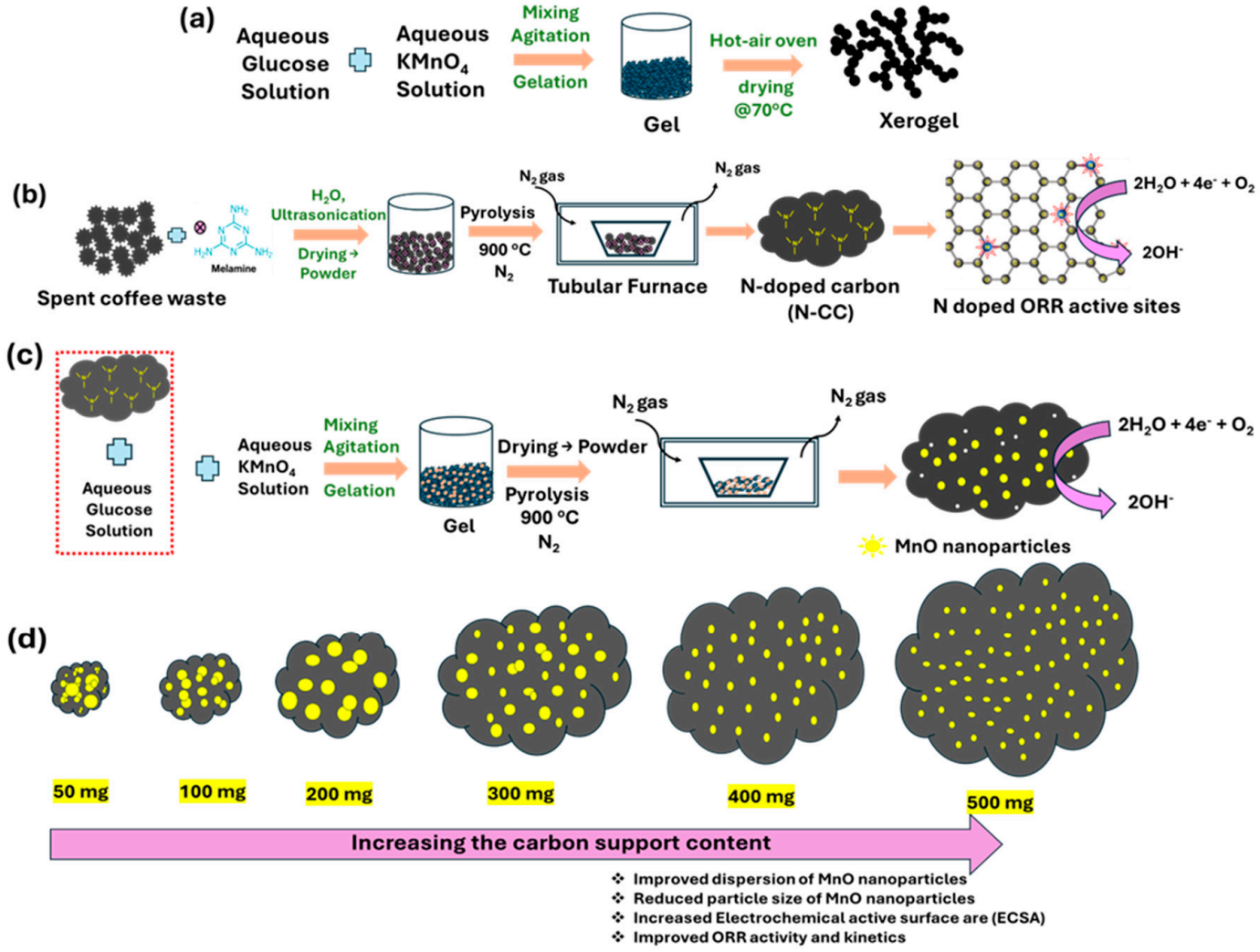

Figure 1. Schematic of (**a**) Mn-Xerogel synthesis, (**b**) synthesis of N-doped carbon from spent coffee waste, (**c**) synthesis of MnO/N-CC catalyst, (**d**) dispersion of MnO nanoparticles on the N-CC carbon support of varying concentrations.

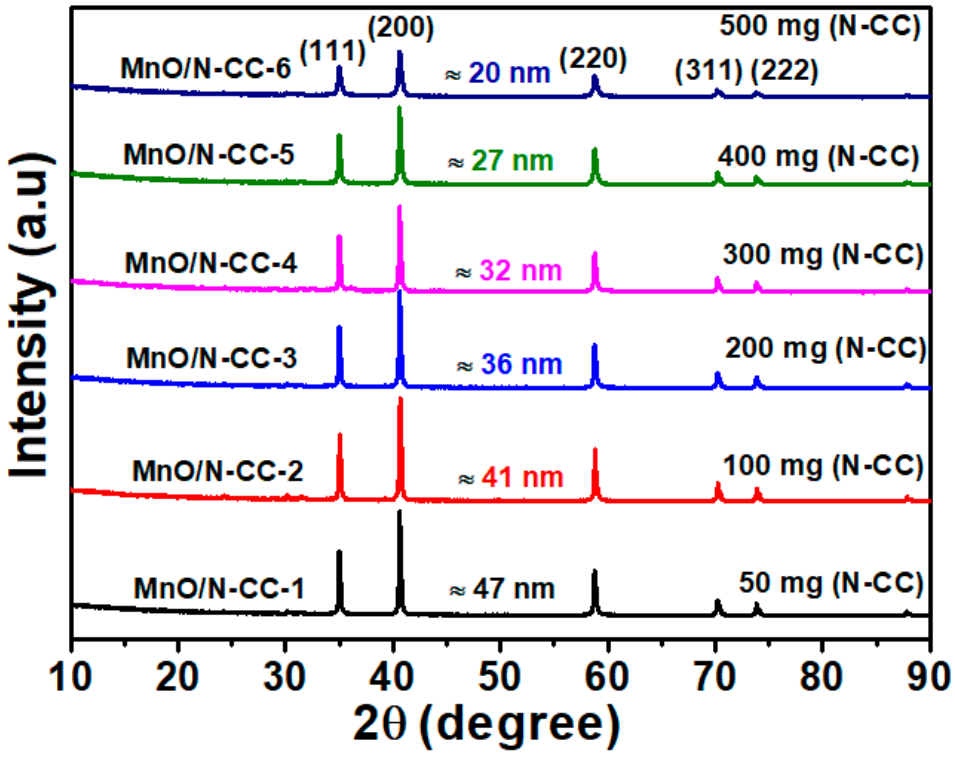

Figure 2. X-ray diffraction patterns of various MnO/N-CC catalysts.

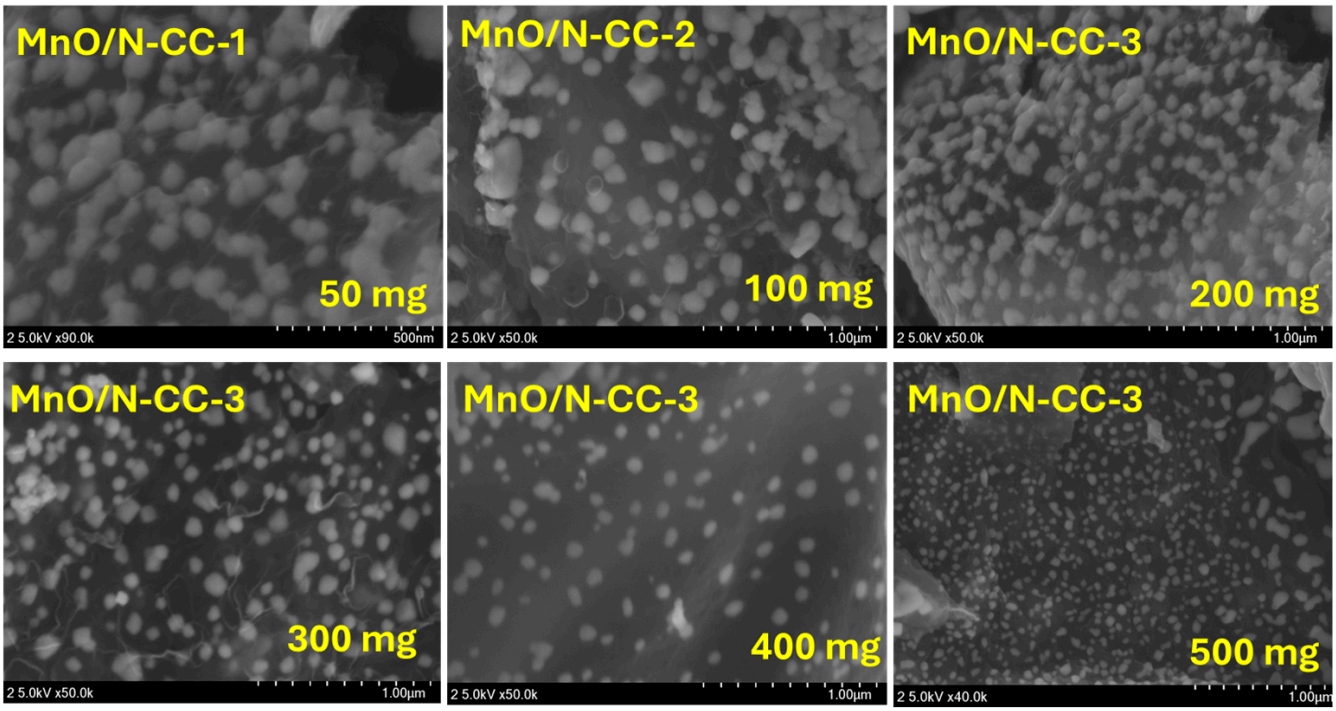

Figure 3. SEM images of various MnO/N-CC catalysts.

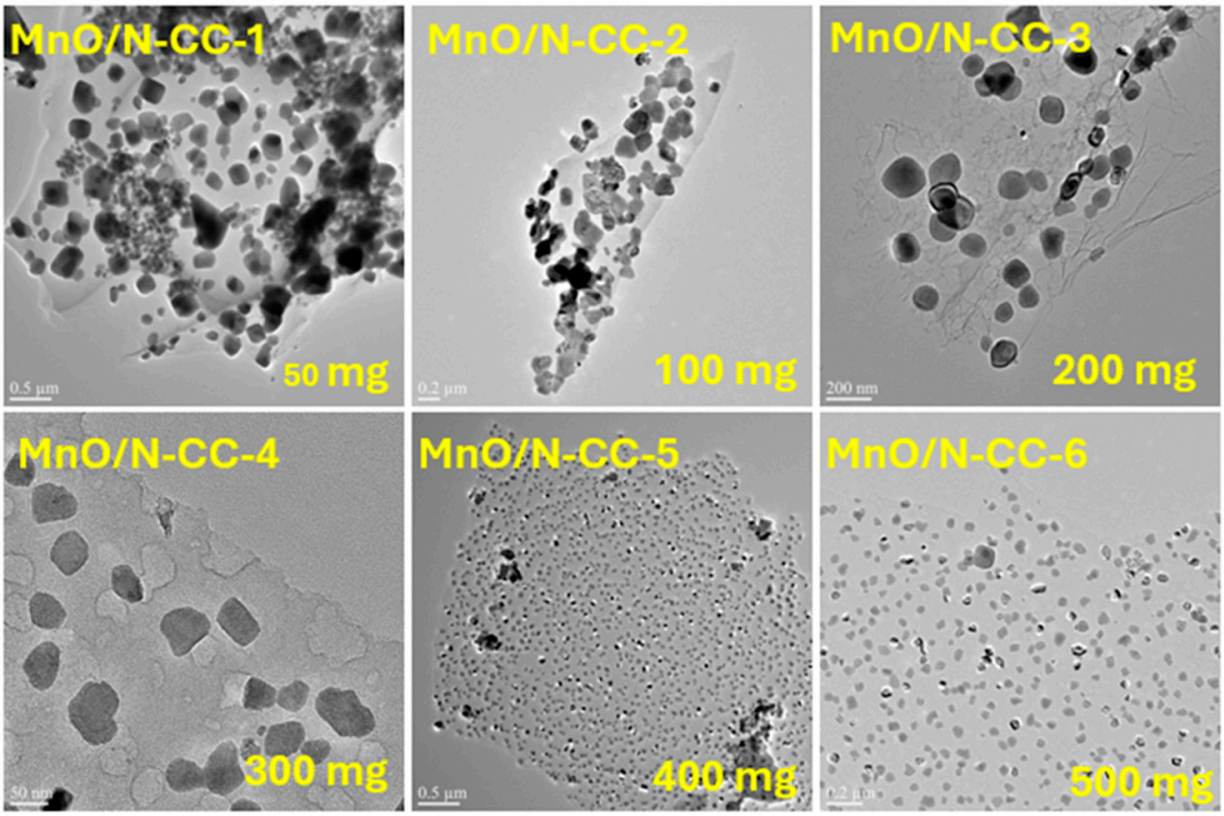

Figure 4. TEM images of various MnO/N-CC catalysts.

2.2. XPS Insights into MnO Nanoparticle Deposition on N-Doped Carbon Supports

Figure S1b shows the survey scan of MnO/N-CC-5 catalyst, which shows the peaks corresponding to C, N, O and Mn elements present in the catalyst. Figure 5a shows the C1s XPS spectra, which can be deconvoluted into four peaks at 283.98, 284.48, 284.88 and 285.78 eV, corresponding to C=C (sp2 carbon), C=C (sp3 carbon), C-N-C (Sp3 carbon), and C-O-C/-C=O functionalities in the carbon matrix derived from the spent coffee carbon+melamine mixture after pyrolysis. The appearance of C-N-C functionalities indicates the presence of N atoms in the carbon matrix and thus confirms -N doping. Figure 5b shows the N1s high-resolution spectra, which can be further deconvoluted into four different N-doping functionalities that can exist in the carbon matrix. The four different peaks located at the binding energies of 398.78, 399.58, 400.68 and 405.99 eV, correspond to pyridinic-N, pyrrolic-N, graphitic-N and pyridinic-Oxidized species, respectively. It is well known that pyridinic-N, pyrrolic-N and graphitic-N are the major N-functionalities that help in ORR. Due to the higher electronegativity of N, the nearby carbon around N becomes electronically deficient, creating partial positive charges on the carbon and partial negative charges on N atoms, indicating less electro-deficient carbon and high-electron-density N species in the carbon atoms [54]. This helps in absorbing gaseous O_2 and its subsequent reduction to H_2O. Therefore, N-doped carbon exhibits high ORR activity in both acidic and alkaline electrolytes. In addition, the N-doping to the carbon enhances the electronic conductivity due to the addition of unpaired electrons from the N into the carbon matrix, which can then be donated to the supported MnO nanoparticles, thus helping in increasing the electron density around the MnO nanoparticles and, in turn, ORR activity [54]. Figure 5c shows the O1s spectra, which can be further deconvoluted into three major peaks at the binding energies of 529.98, 531.38, 532.78 eV, corresponding to Mn-O-Mn, -Mn-O-H/C-O and -C=O oxygen functionalities in the MnO/N-CC-5 catalyst [55]. The appearance of Mn-O-Mn chemical bonding clearly indicates the MnO nanoparticles in the catalyst. Figure 5d shows the Mn2p high-resolution spectra, which is deconvoluted into four major peaks containing two doublet peaks each for Mn2p3/2 and Mn2p1/2. The peaks are located at 640.94

and 642.41, respectively, for Mn^{4+} and Mn^{3+} species of Mn2p3/2 doublet, and 652.58 and 653.93 eV for Mn^{4+} and Mn^{3+} species of Mn2p1/2 doublet [56]. In alkaline electrolytes, the quick reduction of O_2 to OH− ions is guaranteed by the coexistence of Mn^{3+} and Mn^{4+}, which is said to enhance the cleavage of O-O bonds. [47].

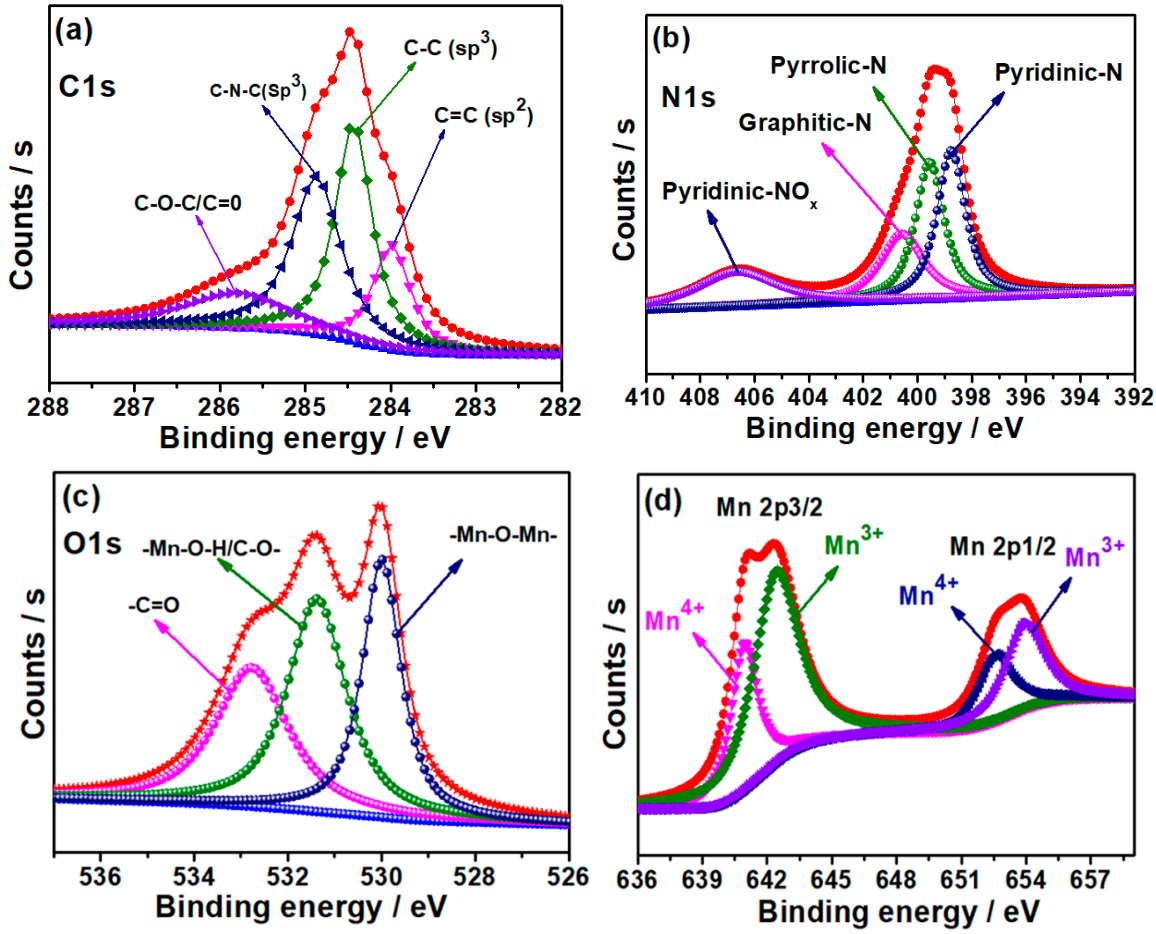

Figure 5. Deconvoluted XPS spectra of (**a**) C1s, (**b**) N1s, (**c**) O1s, and (**d**) Mn2p spectra of MnO/N-CC-5 catalyst.

2.3. Electrochemical ORR Activity Analysis of MnO/N-CC Catalysts

After analyzing the MnO/N-CC catalysts for various physical properties, the electrochemical ORR characterizations of the MnO/N-CC catalyst are performed in 0.1 M KOH electrolyte. Figure 6a shows the recorded LSV curves of MnO/N-CC catalyst in O_2 saturated 0.1 M KOH electrolyte at 1600 rpm. It is seen that all the MnO/N-CC catalysts show typical ORR characteristics with kinetic, a mixed diffusion–kinetic region, and limiting current regions. The optimized ORR activity is illustrated by the half-wave potential ($E_{1/2}$) of various MnO/N-CC catalysts. The obtained $E_{1/2}$ values are 0.65, 0.62, 0.67, 0.69, 0.70, 0.78, 0.71 and 0.81 V vs. RHE, respectively, for N-CC, MnO/N-CC-1, 2, 3, 4, 5, 6 and Pt/C (10 wt.%) catalysts. It is seen that the ORR activity progressively increases with the increase in N-doped carbon content in the catalysts. The optimum ORR activity is obtained for MnO/N-CC-5 catalyst with the highest $E_{1/2}$ potential of 0.78 V vs. RHE. It is interesting to note that the MnO/N-CC-5 catalyst ORR activity is close to the commercial Pt/C catalyst, with just 30 mV lower than Pt/C catalyst (Figure 6b). Further, the Tafel slope values are found to be 248, 150 and 117 mV dec^{-1} for N-CC, MnO/N-CC-5 and Pt/C catalysts, respectively (Figure 6c). These values indicate that the ORR on N-CC catalyst is very sluggish, whereas MnO/N-CC-5 catalyst ORR activity is very much close to the Pt/C catalyst. In order to demonstrate the reason behind the enhanced ORR activity of MnO/N-CC-5, we

have calculated the electrochemical surface area (ECSA) of all the MnO/N-CC catalysts. In order to calculate the ECSA, we have performed CV of the catalysts at various scan rates in the non-Faradaic region and by creating the plots with capacitive current vs. scan rates (Figures S2 and S3). The double-layer capacitance (C_{dl}) is calculated from the slope of the capacitive current (obtained by averaging the anodic and cathodic currents at the selected potential) and then ECSA is calculated by dividing it by the specific capacitance (F/cm^2) of the N-CC carbon [57]. Figure 6d shows the C_{dl}, obtained ECSA values and their relationship with the ORR half-wave potentials. It is clearly seen that with the increase in the N-CC carbon content, the C_{dl} increases steadily, therefore increasing the ECSA values. It can be hypothesized that an increase in N-CC carbon content helps in alleviating the MnO nanoparticle agglomeration, enhances the dispersion and decreases the particle size of MnO nanoparticles, which helps in enhancing the overall ECSA of the catalysts. The optimized catalysts are chosen based on the catalyst that exhibited the highest ORR half-wave potential. According to the table shown in Table S1, MnO/N-CC-5 shows the highest ORR half-wave potential, with ECSA of 4.07 m^2/g. The obtained ECSA values corroborate the XRD, SEM and TEM observations (Figure 6d). Despite the high ECSA of MnO/N-CC-6 catalyst, the ORR activity is observed to be lower than the MnO/N-CC-5 catalysts, and this may be attributable to several reasons. (i) Too small particle size leads to high surface energy and surface defects, which can lead to lower stability, leading to easier agglomeration. (ii) For this reason, making metal nanoparticles smaller does not always help because it changes the shape of the particles and makes more of their less useful surface areas. [58].

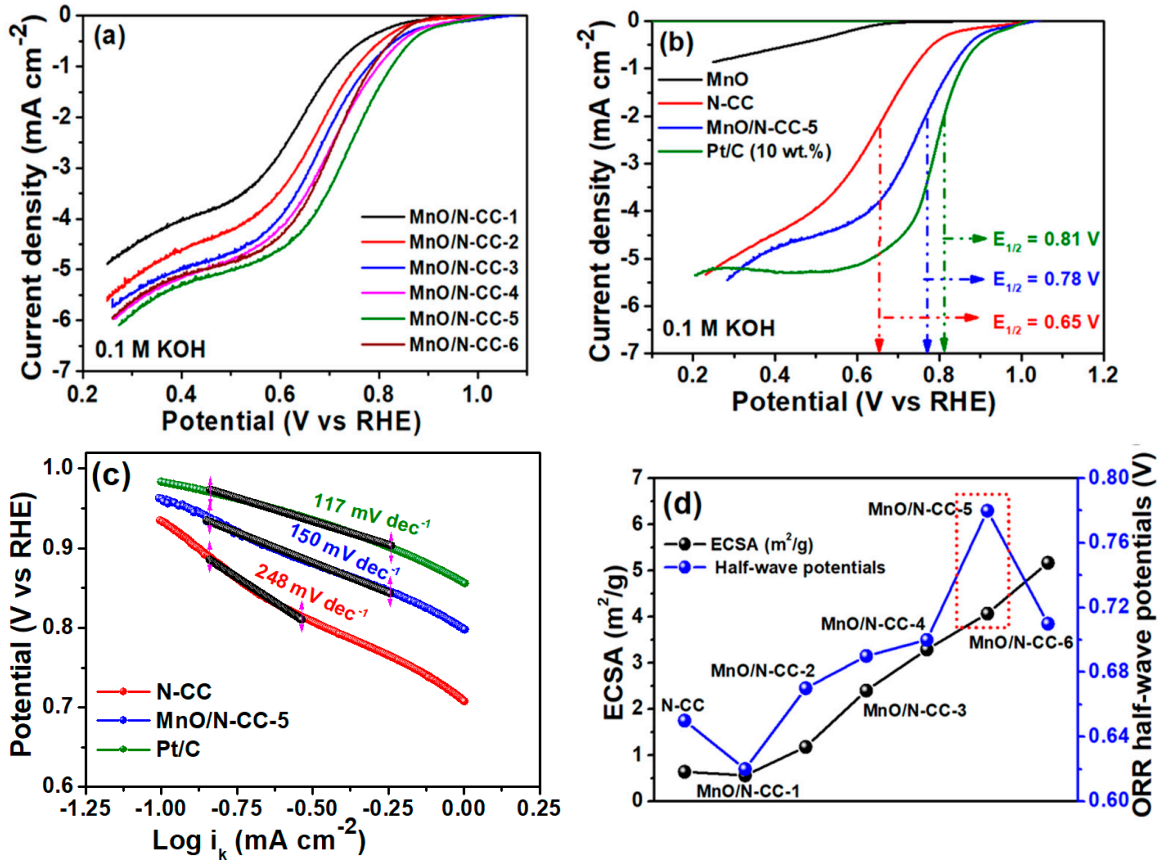

Figure 6. (**a**) LSV curves of various MnO/N-CC catalysts with different N-doped carbon contents, (**b**) comparative LSV curves of MnO, N-CC, MnO-N-CC-5 and Pt/C catalyst, (**c**) Tafel slopes of N-CC, MnO/N-CC-5 and Pt/C catalysts, (**d**) relationships between ECSA and half-wave potentials of the various MnO/N-CC catalysts. Electrolyte: O_2 saturated 0.1 M KOH aqueous solution. Scan rate: 10 mV s^{-1}, 1600 rpm, room temperature (25 °C).

Figure 7a–c show the LSV curves recorded at different rotations per minute (rpm) in O_2-saturated 0.1 M KOH electrolyte of N-CC, MnO-N-CC-5 and Pt/C catalysts, respectively. All the curves show a typical behavior of increased limiting currents with an increase in the rpm. This indicates that the ORR is a diffusion-controlled reaction, meaning that at high rotation speed, the diffused double layer thins, and it allows more O_2 towards the electrode surface, hence the increase in limiting current. This indicates that ORR is limited by the rate at which O_2 diffuses to the electrode surface, rather than the intrinsic kinetic activity. Figure 7d–f represent the Koutecky–Levich (K–L), i.e., the plots of the inverse of square roots of the electrode rotations per min vs. the inverse of the obtained current density. In addition, all the catalysts show linear, straight lines, indicating the possibility of similar number of electrons transferred per O_2 molecule at all the potentials. The number of electrons (n) transferred per O_2 molecule is calculated from the slopes of the K–L plots and incorporating the slope values in the K–L equation (shown in Supplementary Materials). The obtained average 'n' values are 3.61, 3.95, and 3.98 electrons per O_2 molecule, for N-CC, MnO/N-CC-5 and Pt/C (10 wt.%) catalysts, respectively. These results indicate that both MnO/N-CC-5 and Pt/C (10 wt.%) catalysts perform a direct O_2 reduction to H_2O; therefore, they are ideal catalysts for AEM fuel cells.

2.4. Electrochemical Stability Analysis of the Pt/C and MnO/N-CC Catalysts

A catalyst's stability, along with its ORR activity, is a key indicator of its suitability for realistic fuel cells. The stability of the MnO/N-CC-5 catalyst is investigated in two different stability testing conditions: (i) potential cycling and (ii) constant potential conditions. Figure 8 shows the cyclic voltammograms, LSVs and chronoamperometric curves of MnO/N-CC and Pt/C catalysts. The potential cycling of the working electrode deposition with Pt/C and MnO/N-CC-5 catalysts is cycled between 0.05 and 1.23 V vs. RHE in 0.1 M KOH electrolyte for 5000 potential cycles. Figure 8a shows the CV curves of Pt/C catalyst initially and after 5000 potential cycles, and corresponding LSVs recorded after 5000 potential cycles are shown in Figure 8b. The CV of Pt/C shows typical H_{upd} characteristics, and noticeably, after 5000 potential cycles, the Pt/C catalyst area (corresponding to the charge of H_{upd}) under the H_{upd} decreases, suggesting Pt/C catalyst's poor stability. It is well known that Pt/C catalyst undergoes several phenomena, such as carbon corrosion, Pt nanoparticle agglomeration due to Pt atom dissolution and re-deposition, which are major degradation pathways [59]. This is also reflected in the LSV curves recorded after 5000 potential cycles, as shown in Figure 8c. After 5000 potential cycles, the Pt/C catalyst lost 20 mV in its half-wave potentials. In contrast, the MnO/N-CC-5 catalyst shows barely any change in the CV after 5000 potential cycles. This is also reflected in the LSV curves recorded after 5000 potential cycles, as shown in Figure 8d. After 5000 potential cycles, the Pt/C catalyst lost 10 mV in its half-wave potentials, and this indicates that the MnO/N-CC-5 catalyst performs slightly better in terms of stability to potential cycling conditions. The better stability of MnO/N-CC-5 is attributed to the presence of N-doping functionalities, which are known to enhance the stability of the catalyst and help to alleviate the carbon corrosion mechanism [60]. In addition to the potential cycling conditions, the Pt/C and MnO/N-CC-5 catalyst's stability is also evaluated under constant potential conditions by measuring i vs. t curves in 0.1 M KOH electrolyte by holding the potential of the working electrode at 0.7 V vs. RHE for about 10 h with continuous O_2 purging, and the resulting i vs. t curves are shown in Figure 8e. It is clearly seen that after a 10 h test, the Pt/C catalyst retains 94% of the relation current, whereas MnO/N-CC-5 retain about 96% of the relation currents, indicating that both the catalysts show almost similar stability in constant potential conditions. The stability test for MnO/N-CC-5 catalyst is further extended to 24 h, as shown in Figure 8f. The chronoamperometric curves show that MnO/N-CC-5 catalyst proved to have excellent stability, with a current retention of 97.5% after a 24 h test.

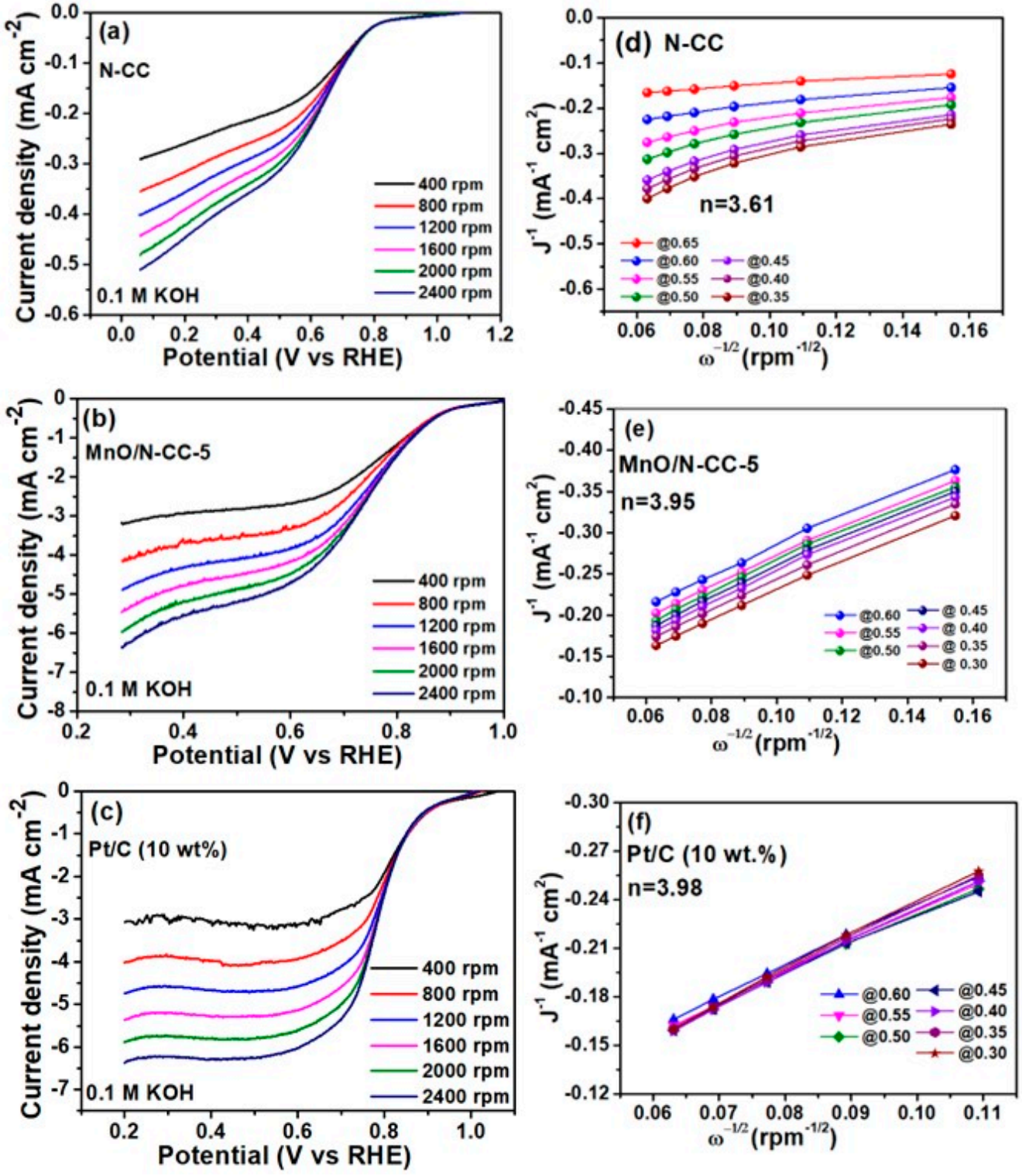

Figure 7. LSV curves recorded at different rpm of (**a**) N-CC, (**b**) MnO/N-CC-5 (**c**) Pt/C and their corresponding K-L plots (**d**) N-CC (**e**) MnO/N-CC-5 and (**f**) Pt/C catalysts. Electrolyte: O_2 saturated 0.1 M KOH aqueous solution. Scan rate: 10 mV s^{-1}, room temperature (~25 °C).

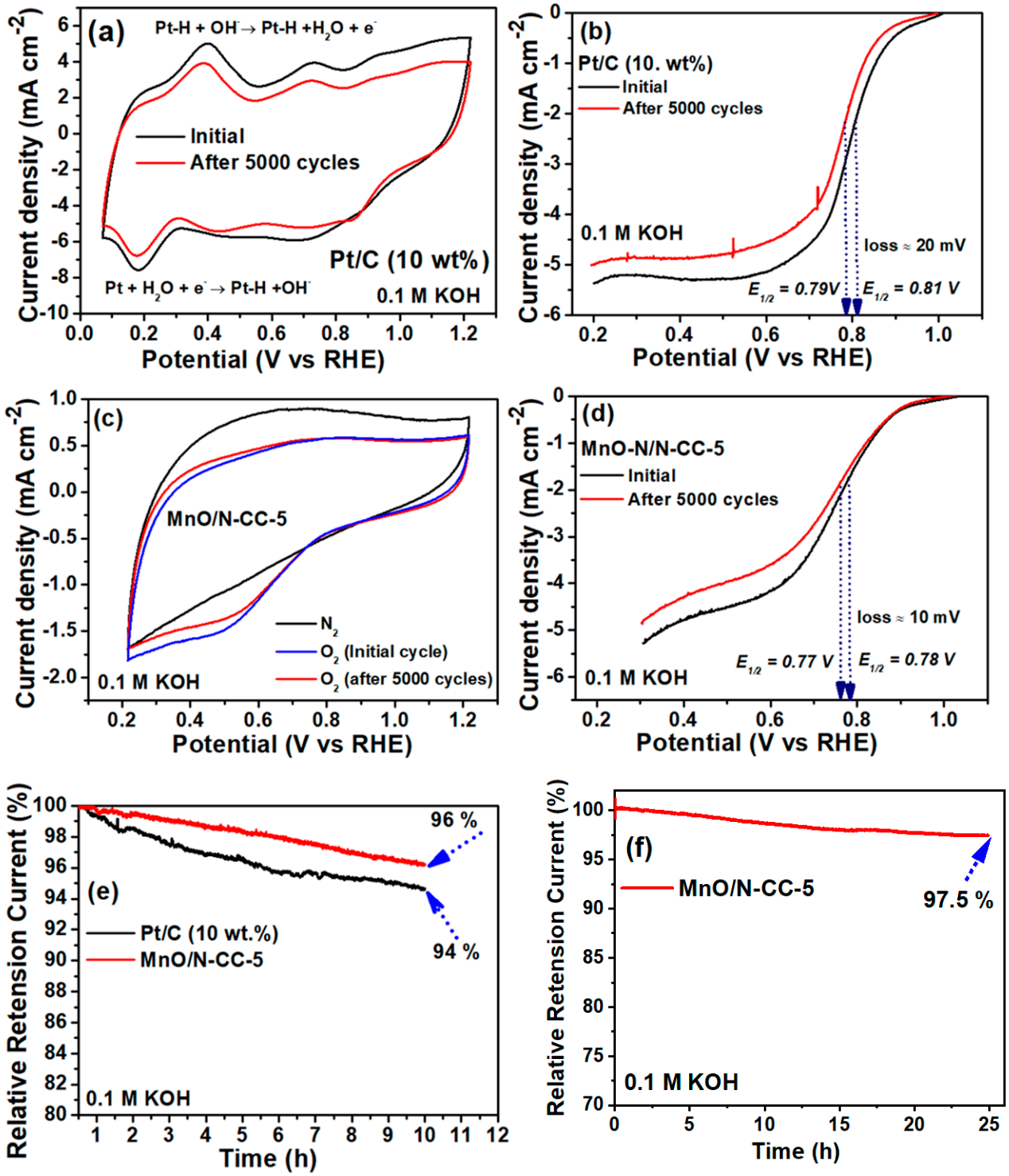

Figure 8. Cyclic voltammograms of (**a**) Pt/C and (**c**) MnO/N-CC-5 catalysts and their corresponding LSV curves; (**b**) Pt/C and (**d**) MnO/N-CC-5 catalysts; (**e**) chronoamperometric response of Pt/C and MnO/N-CC-5 catalysts; (**f**) extended chronoamperometric response of MnO/N-CC-5 catalyst. Electrolyte: N_2/O_2-saturated 0.1 M KOH aqueous solution. Scan rate: 10 mV s^{-1}, 1600 rpm, room temperature (25 °C). Chronoamperometric measurements were conducted in continuous O^2 purging at 0.7 V (vs. RHE) in O_2-saturated 0.1 M KOH electrolyte at a rotating rate of 500 rpm.

2.5. Mechanism of ORR on MnO/N-CC Catalyst

The enhanced ORR activity of Mn(II)O nanoparticles towards ORR is justified on the basis on the ratio of Mn^{3+}/Mn^{4+} and the density functional theory simulation proposed by Tian et al. on ORR activity of Mn(II)O catalysts [47,61]. In general, MOx structural and surface characteristics largely dictate its electrochemical ORR behavior. The fundamental building block of MOx is [MnO_6] octahedrons that are connected in various ways by sharing edges or corners, resulting in structural variations, and the chemical composition of MO_x (more than 20 polymorphs for MO_x are possible) [62]. Because of the redox couple that exists in the octahedral sites with the presence of vacancies in the solid phase, manganese oxides have good electrochemical activity, which can be attributed to Mn^{3+}/Mn^{4+} [63]. The direct four-electron ORR is processed by a chemical oxidation of surface Mn^{3+} generated from MO_x. The ORR activity of MO_x-based catalysts primarily involves the Mn^{3+} ions due to the fact that the Mn^{3+} are unstable due to Jahn–Teller lattice distortions and therefore convert to Mn^{4+} ions, which does not contribute to structural distortion [64]. Therefore, the electron transfer ability of Mn^{3+} to the adsorbed $O_{2(ads)}$-2P orbitals to form Mn^{4+}-$O_{2(ads)}$ is an important characteristic of MO_x catalysts. Hence, the quantity of available Mn^{3+} species on the surface can affect the electro-catalytic activity for ORR of various MO_x catalysts. To gain more insights into the structural composition of Mn^{3+}/Mn^{4+}, we have calculated the area under from the XPS deconvoluted peaks and found that the Mn^{3+}/Mn^{4+} ratio is 1.37, meaning that Mn^{3+} accounts for 37% more than Mn^{4+}. Tian et al. [47] investigated the ORR activity of Mn(II)O catalyst and found that during electrochemical ORR, the Mn(II)O catalyst in situ structurally transform into Mn_5O_8, which reveals the generation and coexistence of Mn^{4+} and Mn^{4+} in the catalyst. The ORR activity of Mn(II)O catalyst is explained on the basis of DFT simulations and the effect of surface Mn^{3+} ions as follows. According to Jahn–Teller lattice distortion theory, the unstable Mn^{3+} will be disproportionate to Mn^{2+} and Mn^{4+} ($2\ Mn^{3+} = Mn^{2+} + Mn^{4+}$) [65]. The antibonding orbitals of Mn^{3+} will overlap directly with that of top-absorbed O species, thus influencing the bonding strength of O_2 onto Mn^{3+} via the filling status [66]. After O_2 absorbs on the surface, sequential electron transfer occurs, leading to the formation of OH^-, as follows (Figure 9).

$$O_2 + \text{Mn-OH} + e^- \rightarrow \text{Mn-OO*} + OH^-$$

$$\text{Mn-OO*} + H_2O + e^- \rightarrow \text{Mn-OOH} + OH^-$$

$$\text{Mn-OOH} + e^- \rightarrow \text{Mn-O} + OH^-$$

$$\text{Mn-O} + H_2O + e^- = \text{Mn-OH} + OH^-$$

Step 1, which involves adsorbing oxygen to replace the OH^- group at the Mn site, is considered the rate-determining step in the kinetics of ORR on Mn(II)O catalyst. Therefore, the enhanced ORR activity of Mn(II)O catalyst is due to optimal adsorption energies of O_2 on Mn^{3+} favoring the cleavage/desorption of OH^- groups from the Mn sites and accelerating the ORR kinetics. In addition, the Mn^{4+} ions also help in scavenging the hydroperoxide (HO_2^-) ions [67]; therefore, a synergistic effect of both Mn^{3+} and Mn^{4+} together with O_2 vacancies accelerates the ORR kinetics [68].

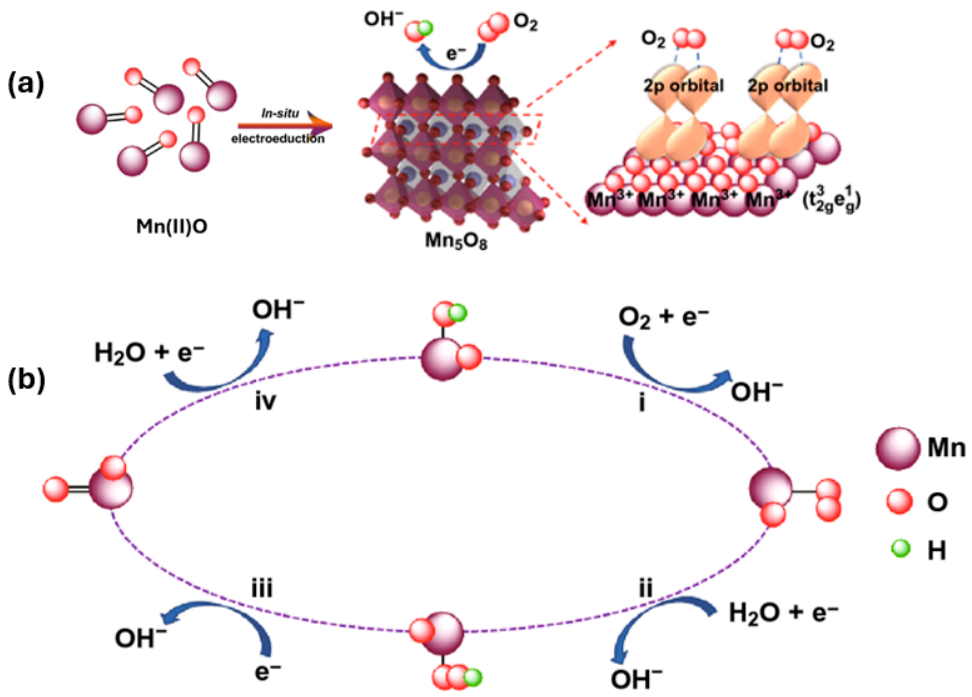

Figure 9. (**a**) Structural evolution schematics of MnO → Mn_5O_8 and the ball–stick model of the O_2 molecule adsorptions on the surface and the lattice structure of Mn_5O_8 (yellow: Mn^{4+}, blue: Mn^{3+}). (**b**) MnO potential four-electron ORR reaction mechanism [concept adopted from Tian et al. [47], open access].

3. Materials and Methods

3.1. Washing of the Spent Coffee Waste

The N-doped carbon is synthesized from spent coffee waste collected from the local coffee shop on the campus of Keimyung University, Daegu, Republic of Korea. First, the collected wet spent coffee grounds (100 g) are dried in the oven at 60 °C, and after its complete drying, the powder is finely ground in a mortar and pestle to crush any large particles. The crushed, powdered, spent coffee grounds are then dispersed in 1000 mL of distilled water and magnetically stirred for about 1 h and the dissolved solids and other soluble impurities are allowed to phase transfer from solid to liquid phase. The dissolved solids can be seen as the water turns a dark brown color. After 1 h, the solution is allowed to stand for the collection of the solid coffee waste at the bottom of the flask and the brown supernatant at the top of the beaker, which is discarded carefully. This entire washing process is repeated several times until all the dissolved solids are removed, and this can be monitored visually when the supernatant water turns clear and colorless. Finally, the collected solid is dried in the oven at 80 °C overnight. The dried spent coffee waste solid is then finely ground in a mortar and pestle. The washed powder is then used for the synthesis of N-doped carbon.

3.2. Synthesis of N-Doped Carbon from the Spent Coffee Waste

The washed spent coffee powder (200 mg) is dispersed in 100 mL of distilled water and ultrasonicated for about 1 h. To this, an equal amount of melamine ($C_3H_6N_6$) (obtained from Sigma-Aldrich®, Seoul, Republic of Korea) powder is added and further ultrasonicated for 1 h and magnetically stirred overnight and then dried in the hot-air oven at 80 °C to evaporate the water, which results in the dried powder, which is then grinded in a mortar and pestle into fine powder. The finely powdered coffee waste and the melamine mixture are then placed in the graphite boat and placed in the center of the tubular furnace. The furnace is connected to the N_2 inert gas, and the furnace is flushed with N_2 initially for about 1 h to replace any O_2 in the tube with N_2. After one hour, the furnace temperature is

raised to 900 °C with a heating rate of 5 °C/min, and once the furnace temperature reaches the target value, the target temperature is maintained for about 1 h, under a continuous flow of N_2 inert gas. The black powder (N-doped carbon, N-CC) resulting from the pyrolysis of the coffee waste and the melamine mixture is collected and grinded in a mortar and pestle into fine powder and then used as carbon support for the deposition of MnO nanoparticles.

3.3. Synthesis of Mn-Xerogel and MnO/N-CC Catalysts

The Mn-Xerogel was synthesized via a sol–gel synthesis technique, according to our previous study [40]. In a typical synthesis, an aqueous solution of potassium permanganate ($KMnO_4$) (obtained from Sigma-Aldrich®, Republic of Korea) is prepared by dissolving 1.50 g in 20 mL of distilled H_2O. In a separate solution, an aqueous solution of D-glucose (obtained from Sigma-Aldrich®, Republic of Korea) is prepared by dissolving 2.51 g of glucose in10 mL of distilled H_2O, to which N-doped carbon in varying quantities is added (50, 100, 200, 300, 400 and 500 mg), and the resulting solution is ultrasonically dispersed for about 1 h and then magnetically stirred for 1 h. In a next step, the D-Glucose + N-CC mixture is added quickly to the aq. $KMnO_4$ solution, and the solution is mixed quickly with the help of a glass rod. With continuous mixing, after approximately 2–3 min, the solution quickly and instantaneously turns into a dark black colored gel. Once the gel had formed, the watery layer on top was formed and it was periodically removed. The beaker with the gel inside was then put into a hot-air oven to dry slowly overnight at ~60 °C. Then, the dried gel was collected from the beaker, and it was transferred into a mortar and pestle and finely grinded into a powder. The powder was then placed into a graphite boat and placed in the center of the tubular furnace. The furnace is connected to the N_2 inert gas, and the furnace is flushed with N_2 initially for about 1 h to replace any O_2 in the tube with N_2. After one hour, the furnace temperature was raised to 900 °C with a heating rate of 5 °C/min, and once the furnace temperature reached the target value, the target temperature was maintained for about 1 h, under a continuous flow of N_2 inert gas. The black powder (MnO/N-CC) resulting from the heat treatment of the MnO-N-CC xerogel was collected and grinded in a mortar and pestle into fine powder and then used as ORR catalyst. The MnO-N-CC xerogels formed with different N-CC contents, i.e., 50, 100, 200, 300, 400 and 500 mg, were also processed in a similar way, and after the heat treatment, they were labelled MnO/N-CC-1, MnO/N-CC-2, MnO/N-CC-3, MnO/N-CC-4, MnO/N-CC-5 and MnO/N-CC-6, respectively.

4. Conclusions

A Xerogel is synthesized using a sol–gel synthesis strategy, and an active and stable catalyst made of transition metal oxide (Mn) is derived from it. This catalyst is supported on a N-doped carbon support that is derived from spent coffee biomass (MnO/N-CC). The purpose of this work is to develop efficient oxygen reduction reaction (ORR) catalysts in alkaline electrolytes. The effects of the carbon content of N-CC on the size of MnO nanoparticles, as well as their dispersion and distribution on N-CC, as well as the morphological and electrochemical effects on ORR, are specifically discussed in detail. Measurements made with a scanning electron microscope and a transmission electron microscope make it abundantly clear that increasing the amount of N-CC present in the MnO gelation reaction leads to an improvement in the MnO dispersion and a reduction in particle size during the thermal treatment process. This, in turn, leads to an increase in the electrochemical active surface area that is available for ORR operations. Several physiochemical and electrochemical characterizations were used to investigate the relationship between the catalyst containing various N-CC and their ORR activities. The results of these investigations revealed a clear relationship between the two. An even distribution of MnO nanoparticles with a crystal size of 27 nm was observed on the N-CC support by the optimal catalyst, which was a MnO/N-CC-5 catalyst. In an electrolyte containing 0.1 M KOH, the MnO/N-CC-5 catalyst displayed ORR kinetics and stability that were almost identical to those of the technologically advanced Pt/C catalyst. Both the half-wave

potential of the optimized MnO/N-CC-5 catalyst, which was 0.78 V vs. RHE, and the ECSA, which was 4.07 m^2/g, were displayed. There was only a loss of 10 mV in half-wave potential after 5000 potential cycles, and the MnO/N-CC-5 catalyst retained 96% of its current for over 18 h of continuous chronoamperometric stability conditions. This is an indication of the catalyst's excellent stability. Based on these findings, it can be concluded that the MnO/N-CC-5 catalyst has the potential to be utilized in energy conversion devices such as fuel cells, metal–air batteries, and biofuel cells as cathode catalysts.

Supplementary Materials: The following supporting information can be downloaded at: https://www.mdpi.com/article/10.3390/catal14110792/s1: The Physical and electrochemical characterizations and electrochemical characterizations of N-CC and MnO/N-CC-catalysts, including, three electrode system measurements, ORR activity analysis in 0.1 M KOH electrolyte, RDE at different rotation speeds, K-L plots calculations, ECSA calculations and their relation experimental and equations are given in the supporting Information of this article. S1. Physical and electrochemical characterizations, S2. Electrochemical Characterizations of the N-CC and MnO/N-CC catalysts, Figure S1, (a) XRD patterns of washed spent coffee waste and after pyrolysis (b) XPS survey spectrum of MnO/N-CC-5 catalysts, Figure S2. CV curves of various MnO/N-CC catalysts in N2 saturated 0.1 M KOH electrolyte with different scan rates. Figure S3. Plots of capacitive currents vs scan rates of various MnO/N-CC derived from the cyclic voltammograms. Table S1. Relationship between ECSA and half-wave potential of various MnO/N-CC catalysts.

Author Contributions: Conceptualization, S.G.P.; Funding acquisition, S.G.P. and A.N.A.; Investigation, G.K.; Methodology, S.G.P. and R.K.; Resources, G.K., A.N.A. and S.W.K.; Software, P.S.P.R.; Writing—original draft, S.G.P. and R.K.; Writing—review and editing, A.N.A., S.P. and M.R.T. All authors have read and agreed to the published version of the manuscript.

Funding: The research was supported by the National Research Foundation of Korea (NRF) funded by the Korean Government, Ministry of Science and ICT (MSIT) (No. 2021R1F1A1046648), Republic of Korea. The authors acknowledge Researchers Supporting Project Number (RSP2024R304), King Saud University, Riyadh, Saudi Arabia.

Data Availability Statement: The original contributions presented in this study are included in the article/Supplementary Materials. Further inquiries can be directed to the corresponding authors.

Conflicts of Interest: The authors declare no conflicts of interest.

References

1. Yan, J.; Jing, J.; Li, Y. Hydrogen fuel cell commercial vehicles in China: Evaluation of carbon emission reduction and its economic value. *Int. J. Hydrogen Energy* **2023**, *52*, 734–749. [CrossRef]
2. Xu, X.; Dong, Y.; Hu, Q.; Si, N.; Zhang, C. Electrochemical Hydrogen Storage Materials: State-of-the-Art and Future Perspectives. *Energy Fuels* **2024**, *38*, 7579–7613. [CrossRef]
3. Zheng, D.; Liu, K.; Zhang, Z.; Fu, Q.; Bian, M.; Han, X.; Shen, X.; Chen, X.; Xie, H.; Wang, X.; et al. Essential features of weak current for excellent enhancement of NOx reduction over monoatomic V-based catalyst. *Nat. Commun.* **2024**, *15*, 6688. [CrossRef] [PubMed]
4. Luo, P.; Huang, Z.; Wang, T.; Xiao, H.; Ma, X.; Yan, R.; Zhao, G. Design and fabrication of nitrogen-doped graphene-promoted $Na_3MnTi(PO_4)_3$@C cathode with three-electron reactions for sodium-ion storage. *Solid State Sci.* **2024**, *156*, 107678. [CrossRef]
5. Qian, Q.; Zhu, Y.; Ahmad, N.; Feng, Y.; Zhang, H.; Cheng, M.; Liu, H.; Xiao, C.; Zhang, G.; Xie, Y. Recent Advancements in Electrochemical Hydrogen Production via Hybrid Water Splitting. *Adv. Mater.* **2023**, *36*, e2306108. [CrossRef] [PubMed]
6. Ding, X.; Fan, Y.; Zhang, Z.; Chen, D.; Yao, S. Lattice Boltzmann simulation of ion transport during the charging process of porous electrodes in randomly reconstructed seawater desalination batteries. *Int. Commun. Heat Mass Transf.* **2024**, *159*, 107942. [CrossRef]
7. Sun, H.; Xu, X.; Fei, L.; Zhou, W.; Shao, Z. Electrochemical Oxidation of Small Molecules for Energy-Saving Hydrogen Production. *Adv. Energy Mater.* **2024**, *14*, 2401242. [CrossRef]
8. Xu, X.; Pan, Y.; Zhong, Y.; Ran, R.; Shao, Z. Ruddlesden–Popper perovskites in electrocatalysis. *Mater. Horiz.* **2020**, *7*, 2519–2565. [CrossRef]
9. Halder, P.; Babaie, M.; Salek, F.; Haque, N.; Savage, R.; Stevanovic, S.; Bodisco, T.A.; Zare, A. Advancements in hydrogen production, storage, distribution and refuelling for a sustainable transport sector: Hydrogen fuel cell vehicles. *Int. J. Hydrogen Energy* **2023**, *52*, 973–1004. [CrossRef]
10. Halder, P.; Babaie, M.; Salek, F.; Shah, K.; Stevanovic, S.; Bodisco, T.A.; Zare, A. Performance, emissions and economic analyses of hydrogen fuel cell vehicles. *Renew. Sustain. Energy Rev.* **2024**, *199*, 114543. [CrossRef]

11. Sun, Y.; Polani, S.; Luo, F.; Ott, S.; Strasser, P.; Dionigi, F. Advancements in cathode catalyst and cathode layer design for proton exchange membrane fuel cells. *Nat. Commun.* **2021**, *12*, 5984. [CrossRef] [PubMed]
12. Li, J.; Liu, M.; Liu, X.; Yu, X.; Li, Q.; Sun, Q.; Sun, T.; Cao, S.; Hou, C. The Recent Progress of Oxygen Reduction Electrocatalysts Used at Fuel Cell Level. *Small Methods* **2023**, *8*, e2301249. [CrossRef] [PubMed]
13. Zhou, Z.; Zhang, H.-J.; Feng, X.; Ma, Z.; Ma, Z.-F.; Xue, Y. Progress of Pt and iron-group transition metal alloy catalysts with high ORR activity for PEMFCs. *J. Electroanal. Chem.* **2024**, *959*, 118165. [CrossRef]
14. Yi, S.; Song, X.; Shen, Y.; Xu, R.; Zhao, Y.; Chen, P. Research progress in alloy catalysts for oxygen reduction reaction. *J. Alloys Compd.* **2024**, *1002*, 175258. [CrossRef]
15. Burke, A.F.; Zhao, J.; Fulton, L.M. Projections of the costs of light-duty battery-electric and fuel cell vehicles (2020–2040) and related economic issues. *Res. Transp. Econ.* **2024**, *105*, 101440. [CrossRef]
16. Li, F.; Chan, S.H.; Tu, Z. Recent Development of Anion Exchange Membrane Fuel Cells and Performance Optimization Strategies: A Review. *Chem. Rec.* **2023**, *24*, e202300067. [CrossRef] [PubMed]
17. Wu, H.; Chen, M.; Li, W.; Lu, B. Recent Progress on Durable Metal-N-C Catalysts for Proton Exchange Membrane Fuel Cells. *Chem.-Asian J.* **2023**, *19*, e202300862. [CrossRef] [PubMed]
18. Yuan, Y.; Zheng, Y.; Luo, D.; Qiu, W.; Wang, J.; Wang, X.; Chen, Z. Recent progress on mechanisms, principles, and strategies for high-activity and high-stability non-PGM fuel cell catalyst design. *Carbon Energy* **2024**, *6*, e426. [CrossRef]
19. Huang, J.; Zhang, Q.; Ding, J.; Zhai, Y. Fe–N–C single atom catalysts for the electrochemical conversion of carbon, nitrogen and oxygen elements. *Mater. Rep. Energy* **2022**, *2*, 100141. [CrossRef]
20. Krishnan, S.R.; Verstraete, D.; Aguey-Zinsou, F. Performance of Non-Precious Metal Electrocatalysts in Proton-Exchange Membrane Fuel Cells: A Review. *ChemElectroChem* **2024**, *11*, e202400299. [CrossRef]
21. Qu, X.; Yan, Y.; Zhang, Z.; Tian, B.; Yin, S.; Cheng, X.; Huang, R.; Jiang, Y.; Sun, S. Regulation Strategies for Fe−N−C and Co−N−C Catalysts for the Oxygen Reduction Reaction. *Chem.-Eur. J.* **2024**, *30*, e202304003. [CrossRef]
22. Zhu, Y.; Zhang, B.; Wang, D.; Su, D.S. Order of Activity of Nitrogen, Iron Oxide, and FeN_x Complexes towards Oxygen Reduction in Alkaline Medium. *ChemSusChem* **2015**, *8*, 4016–4021. [CrossRef] [PubMed]
23. Chen, S.; Xu, Q.; Sun, H.; Ge, L.; Huang, D.; Zhang, Z.; Qiao, Y.; Tong, X.; Fan, W. Cobalt-Embedded Nitrogen-Doped Carbon Nanosheets for Oxygen Reduction Reaction under Alkaline and Acidic Media. *ACS Appl. Nano Mater.* **2024**, *7*, 15710–15719. [CrossRef]
24. Morankar, A.; Atanassov, P.; Greeley, J. Hydrogen Peroxide-Induced Overoxidation of Fe−N−C Catalysts: Implications for ORR Activity. *Chemphyschem* **2024**, *25*, e202400199. [CrossRef]
25. Yue, X.; Liu, Y.; Lu, B.; Du, X.; Lei, W.; Liu, Z.; Yi, S.; Lu, C. Inherent anti-Fenton property of single-atom rhenium for the ultra-durable oxygen reduction reaction. *Energy Environ. Sci.* **2024**, *17*, 5892–5900. [CrossRef]
26. Peera, S.G.; Liu, C.; Asokan, A.; Suss, M.E. Cu@NC as high-performance and durable electrocatalyst for oxygen reduction reaction in alkaline membrane fuel cells. *J. Alloys Compd.* **2022**, *938*, 168636. [CrossRef]
27. Kisand, K.; Sarapuu, A.; Akula, S.; Kikas, A.; Treshchalov, A.; Käärik, M.; Piirsoo, H.-M.; Kozlova, J.; Aruväli, J.; Leis, J.; et al. Iron and manganese co-doped mesoporous carbon-based catalysts via template-assisted synthesis for proton exchange membrane fuel cells. *J. Power Sources* **2024**, *618*, 235166. [CrossRef]
28. Khater, D.Z.; Amin, R.S.; Mahmoud, M.; El-Khatib, K.M. Evaluation of mixed transition metal (Co, Mn, and Cu) oxide electrocatalysts anchored on different carbon supports for robust oxygen reduction reaction in neutral media. *RSC Adv.* **2022**, *12*, 2207–2218. [CrossRef] [PubMed]
29. Speck, F.D.; Santori, P.G.; Jaouen, F.; Cherevko, S. Mechanisms of Manganese Oxide Electrocatalysts Degradation during Oxygen Reduction and Oxygen Evolution Reactions. *J. Phys. Chem. C* **2019**, *123*, 25267–25277. [CrossRef]
30. Li, Y.; Chen, M.; Lu, B.; Wu, H.; Zhang, J. Unravelling the role of hydrogen peroxide in pH-dependent ORR performance of Mn-N-C catalysts. *Appl. Catal. B Environ.* **2023**, *342*, 123458. [CrossRef]
31. Kumar, N.; Shaik, G.P.; Pandurangan, S.; Khalkho, B.; Neelakantan, L.; Chetty, R. Corrosion characteristics and fuel cell performance of a cost-effective high Mn–Low Ni austenitic stainless steel as an alternative to SS 316L bipolar plate. *Int. J. Energy Res.* **2020**, *44*, 6804–6818. [CrossRef]
32. Dessie, Y.; Tadesse, S.; Eswaramoorthy, R.; Abebe, B. Recent developments in manganese oxide based nanomaterials with oxygen reduction reaction functionalities for energy conversion and storage applications: A review. *J. Sci. Adv. Mater. Devices* **2019**, *4*, 353–369. [CrossRef]
33. Parveen, N.; Ansari, S.A.; Ansari, M.Z.; Ansari, M.O. Manganese oxide as an effective electrode material for energy storage: A review. *Environ. Chem. Lett.* **2021**, *20*, 283–309. [CrossRef]
34. Yuan, H.; Deng, L.; Tang, J.; Zhou, S.; Chen, Y.; Yuan, Y. Facile Synthesis of MnO_2/Polypyrrole/MnO_2Multiwalled Nanotubes as Advanced Electrocatalysts for the Oxygen Reduction Reaction. *ChemElectroChem* **2015**, *2*, 1152–1158. [CrossRef]
35. Hu, K.; Xiao, X.; Du, P.; Yang, H.; Shen, Z.; Jin, G.; Wang, F.; Pan, F.; Zhao, Q.; Lou, Z. Facile fabrication of Mn-N doped porous carbon nanocages with enhanced oxygen reduction reaction activity. *J. Alloys Compd.* **2023**, *967*, 171819. [CrossRef]
36. Sun, Y.; Ding, S.; Xia, B.; Duan, J.; Antonietti, M.; Chen, S. Biomimetic FeMo(Se, Te) as Joint Electron Pool Promoting Nitrogen Electrofixation. *Angew. Chem. Int. Ed.* **2022**, *61*, e202115198. [CrossRef]
37. Peera, S.G.; Koutavarapu, R.; Akula, S.; Asokan, A.; Moni, P.; Selvaraj, M.; Balamurugan, J.; Kim, S.O.; Liu, C.; Sahu, A.K. Carbon Nanofibers as Potential Catalyst Support for Fuel Cell Cathodes: A Review. *Energy Fuels* **2021**, *35*, 11761–11799. [CrossRef]

38. Wan, X.; Zhao, Y.; Li, Z.; Li, L. Emerging polymeric electrospun fibers: From structural diversity to application in flexible bioelectronics and tissue engineering. *Exploration* **2022**, *2*, 20210029. [CrossRef] [PubMed]
39. Krishna, A.M.S.; Ramasubramanian, B.; Haseena, S.; Bamola, P.; Sharma, H.; Mahata, C.; Chroneos, A.; Krishnamurthy, S.; Ravva, M.K.; Chandu, B.; et al. Functionalized Graphene-Incorporated Cupric Oxide Charge-Transport Layer for Enhanced Photoelectrochemical Performance and Hydrogen Evolution. *Catalysts* **2023**, *13*, 785. [CrossRef]
40. Dessalle, A.; Quílez-Bermejo, J.; Fierro, V.; Xu, F.; Celzard, A. Recent progress in the development of efficient biomass-based ORR electrocatalysts. *Carbon* **2022**, *203*, 237–260. [CrossRef]
41. Cao, Y.; Sun, Y.; Zheng, R.; Wang, Q.; Li, X.; Wei, H.; Wang, L.; Li, Z.; Wang, F.; Han, N. Biomass-derived carbon material as efficient electrocatalysts for the oxygen reduction reaction. *Biomass-Bioenergy* **2022**, *168*, 106676. [CrossRef]
42. Yin, S.; Du, Y.; Liang, X.; Xie, Y.; Xie, D.; Mei, Y. Surface coating of biomass-modified black phosphorus enhances flame retardancy of rigid polyurethane foam and its synergistic mechanism. *Appl. Surf. Sci.* **2023**, *637*, 157961. [CrossRef]
43. Mehmandoust, M.; Li, G.; Erk, N. Biomass-Derived Carbon Materials as an Emerging Platform for Advanced Electrochemical Sensors: Recent Advances and Future Perspectives. *Ind. Eng. Chem. Res.* **2022**, *62*, 4628–4635. [CrossRef]
44. Pagett, M.; Teng, K.S.; Sullivan, G.; Zhang, W. Reusing Waste Coffee Grounds as Electrode Materials: Recent Advances and Future Opportunities. *Glob. Chall.* **2022**, *7*, 2200093. [CrossRef] [PubMed]
45. Tiwari, S.K.; Bystrzejewski, M.; De Adhikari, A.; Huczko, A.; Wang, N. Methods for the conversion of biomass waste into value-added carbon nanomaterials: Recent progress and applications. *Prog. Energy Combust. Sci.* **2022**, *92*, 101023. [CrossRef]
46. Hao, W.; Lee, S.-H.; Peera, S.G. Xerogel-Derived Manganese Oxide/N-Doped Carbon as a Non-Precious Metal-Based Oxygen Reduction Reaction Catalyst in Microbial Fuel Cells for Energy Conversion Applications. *Nanomaterials* **2023**, *13*, 2949. [CrossRef] [PubMed]
47. Tian, H.; Zeng, L.; Huang, Y.; Ma, Z.; Meng, G.; Peng, L.; Chen, C.; Cui, X.; Shi, J. In Situ Electrochemical Mn(III)/Mn(IV) Generation of Mn(II)O Electrocatalysts for High-Performance Oxygen Reduction. *Nano-Micro Lett.* **2020**, *12*, 161. [CrossRef] [PubMed]
48. Arunchander, A.; Vivekanantha, M.; Peera, S.G.; Sahu, A.K. MnO–nitrogen doped graphene as a durable non-precious hybrid catalyst for the oxygen reduction reaction in anion exchange membrane fuel cells. *RSC Adv.* **2016**, *6*, 95590–95600. [CrossRef]
49. Isaifan, R.J.; Ntais, S.; Baranova, E.A. Particle size effect on catalytic activity of carbon-supported Pt nanoparticles for complete ethylene oxidation. *Appl. Catal. A Gen.* **2013**, *464–465*, 87–94. [CrossRef]
50. Nguyen, V.T.; Fitzgerald, M.A.; Ibbotson, D.; Foster, J.; Dzara, M.J.; Zaccarine, S.F.; Vyas, S.; Pylypenko, S. Effects of Graphitic and Pyridinic Nitrogen Defects on Transition Metal Nucleation and Nanoparticle Formation on N-Doped Carbon Supports: Implications for Catalysis. *ACS Appl. Nano Mater.* **2022**, *5*, 14922–14933. [CrossRef]
51. Hornberger, E.; Merzdorf, T.; Schmies, H.; Hübner, J.; Klingenhof, M.; Gernert, U.; Kroschel, M.; Anke, B.; Lerch, M.; Schmidt, J.; et al. Impact of Carbon N-Doping and Pyridinic-N Content on the Fuel Cell Performance and Durability of Carbon-Supported Pt Nanoparticle Catalysts. *ACS Appl. Mater. Interfaces* **2022**, *14*, 18420–18430. [CrossRef] [PubMed]
52. Wu, X.; Wang, Z.; Chen, K.; Li, Z.; Hu, B.; Wang, L.; Wu, M. Unravelling the Role of Strong Metal–Support Interactions in Boosting the Activity toward Hydrogen Evolution Reaction on Ir Nanoparticle/N-Doped Carbon Nanosheet Catalysts. *ACS Appl. Mater. Interfaces* **2021**, *13*, 22448–22456. [CrossRef] [PubMed]
53. Li, P.; Wen, J.; Xiang, Y.; Li, M.; Zhao, Y.; Wang, S.; Dou, J.; Li, Y.; Ma, H.; Xu, L. Hierarchical mesoporous N-doped carbon as an efficient ORR/OER bifunctional electrocatalyst for rechargeable zinc–air battery. *Inorg. Chem. Front.* **2024**, *11*, 5345–5358. [CrossRef]
54. Ma, R.; Lin, G.; Zhou, Y.; Liu, Q.; Zhang, T.; Shan, G.; Yang, M.; Wang, J. A review of oxygen reduction mechanisms for metal-free carbon-based electrocatalysts. *npj Comput. Mater.* **2019**, *5*, 78. [CrossRef]
55. Xie, G.; Liu, X.; Li, Q.; Lin, H.; Li, Y.; Nie, M.; Qin, L. The evolution of α-MnO_2 from hollow cubes to hollow spheres and their electrochemical performance for supercapacitors. *J. Mater. Sci.* **2017**, *52*, 10915–10926. [CrossRef]
56. Wang, M.; Chen, K.; Liu, J.; He, Q.; Li, G.; Li, F. Efficiently Enhancing Electrocatalytic Activity of α-MnO_2 Nanorods/N-Doped Ketjenblack Carbon for Oxygen Reduction Reaction and Oxygen Evolution Reaction Using Facile Regulated Hydrothermal Treatment. *Catalysts* **2018**, *8*, 138. [CrossRef]
57. Qaseem, A.; Chen, F.; Wu, X.; Zhang, N.; Xia, Z. Ag, Co/graphene interactions and its effect on electrocatalytic oxygen reduction in alkaline media. *J. Power Sources* **2017**, *370*, 1–13. [CrossRef]
58. Leontyev, I.N.; Belenov, S.V.; Guterman, V.E.; Haghi-Ashtiani, P.; Shaganov, A.P.; Dkhil, B. Catalytic Activity of Carbon-Supported Pt Nanoelectrocatalysts. Why Reducing the Size of Pt Nanoparticles is Not Always Beneficial. *J. Phys. Chem. C* **2011**, *115*, 5429–5434. [CrossRef]
59. Zadick, A.; Dubau, L.; Sergent, N.; Berthomé, G.; Chatenet, M. Huge Instability of Pt/C Catalysts in Alkaline Medium. *ACS Catal.* **2015**, *5*, 4819–4824. [CrossRef]
60. Li, Y.; Li, J.; Wang, Y.; Chen, X.; Liu, M.; Zheng, Z.; Peng, X. Carbon corrosion mechanism on nitrogen-doped carbon support—A density functional theory study. *Int. J. Hydrogen Energy* **2021**, *46*, 13273–13282. [CrossRef]
61. Li, Z.; Yang, Y.; Relefors, A.; Kong, X.; Siso, G.M.; Wickman, B.; Kiros, Y.; Soroka, I.L. Tuning morphology, composition and oxygen reduction reaction (ORR) catalytic performance of manganese oxide particles fabricated by γ-radiation induced synthesis. *J. Colloid Interface Sci.* **2021**, *583*, 71–79. [CrossRef] [PubMed]

62. Robinson, D.M.; Go, Y.B.; Mui, M.; Gardner, G.; Zhang, Z.; Mastrogiovanni, D.; Garfunkel, E.; Li, J.; Greenblatt, M.; Dismukes, G.C. Photochemical Water Oxidation by Crystalline Polymorphs of Manganese Oxides: Structural Requirements for Catalysis. *J. Am. Chem. Soc.* **2013**, *135*, 3494–3501. [CrossRef] [PubMed]
63. Brenet, J. Electrochemical behaviour of metallic oxides. *J. Power Sources* **1979**, *4*, 183–190. [CrossRef]
64. Zhang, Q.; Didier, C.; Pang, W.K.; Liu, Y.; Wang, Z.; Li, S.; Peterson, V.K.; Mao, J.; Guo, Z. Structural Insight into Layer Gliding and Lattice Distortion in Layered Manganese Oxide Electrodes for Potassium-Ion Batteries. *Adv. Energy Mater.* **2019**, *9*, 1900568. [CrossRef]
65. Takashima, T.; Hashimoto, K.; Nakamura, R. Inhibition of Charge Disproportionation of MnO_2 Electrocatalysts for Efficient Water Oxidation Under Neutral Conditions. *J. Am. Chem. Soc.* **2012**, *134*, 18153–18156. [CrossRef] [PubMed]
66. Stoerzinger, K.A.; Risch, M.; Han, B.; Shao-Horn, Y. Recent Insights into Manganese Oxides in Catalyzing Oxygen Reduction Kinetics. *ACS Catal.* **2015**, *5*, 6021–6031. [CrossRef]
67. Chinnadurai, D.; Nallal, M.; Kim, H.; Li, O.L.; Park, K.H.; Prabakar, K. Mn^{3+} Active Surface Site Enriched Manganese Phosphate Nano-polyhedrons for Enhanced Bifunctional Oxygen Electrocatalyst. *ChemCatChem* **2020**, *12*, 2348–2355. [CrossRef]
68. Shi, J. On the Synergetic Catalytic Effect in Heterogeneous Nanocomposite Catalysts. *Chem. Rev.* **2012**, *113*, 2139–2181. [CrossRef] [PubMed]